Research in Astronomy and Astrophysics, 24:045007 (7pp), 2024 April https://doi.org/10.1088/1674-4527/ad304c

Four Late-type Galaxies with Double Radio Lobes and Properties of Such Galaxies

Z. S. Yuan[1,2], X. Y. Gao[1,2,3], Z. L. Wen[1,2], and J. L. Han[1,2,3]
[1] National Astronomical Observatories, Chinese Academy of Sciences, Beijing 100101, China; zsyuan@nao.cas.cn
[2] CAS Key Laboratory of FAST, National Astronomical Observatories, Chinese Academy of Sciences, Beijing 100101, China
[3] School of Astronomy and Space Sciences, University of Chinese Academy of Sciences, Beijing 100049, China
Received 2023 December 18; revised 2024 February 20; accepted 2024 February 29; published 2024 March 27

Abstract

The triggering mechanism for radio lobes from late-type galaxies is not fully understood. More samples are desired for a thorough investigation and statistics. By utilizing the optical data from the newly released Dark Energy Spectroscopic Instrument imaging surveys and the radio sources from the NRAO VLA Sky Survey and the Faint Images of the Radio Sky at Twenty-centimeter, we identify four Late-type Galaxies with double Radio Lobes (LaGRLs): J0217−3645, J0947+6220, J1412+3723 and J1736+5108. Including previously known LaGRLs, we confirm the correlation between radio power $P_{1.4\,\mathrm{GHz}}$ and stellar mass M_* of host galaxies. Most (25/35) LaGRLs belong to the blue cloud galaxies, while the newly identified cases in this work are located within the region of the red sequence. We find a clear correlation between the differential radio power, i.e., the offset from the $P_{1.4\,\mathrm{GHz}} - M_*$ relation, and the galaxy color, indicating that bluer galaxies at a fixed M_* tend to host more powerful radio lobes. Furthermore, the majority (31/36) of LaGRLs are either located in a galaxy group or displaying a disturbed morphology. We suggest that all of the galaxy mass, color and surrounding environment could play important roles in triggering radio lobes in late-type galaxies.

Key words: galaxies: active – galaxies: jets – galaxies: spiral – radio continuum: galaxies

1. Introduction

Powerful radio jets or lobes have been conventionally thought to be associated with early-type galaxies, rather than late-type galaxies, since the latter are considered less likely to host a central black hole (BH) with sufficient mass (typically $M_\bullet > 10^8 M_\odot$) to produce such jets or lobes (e.g., Véron-Cetty & Véron 2001; Best et al. 2005). However, this perception is gradually changed owing to the discovery of disk or spiral galaxies hosting double radio lobes, i.e., 0313−192, a standard edge-on disk galaxy with radio lobes extending to ∼200 kpc (Ledlow et al. 1998, 2001; Keel et al. 2006), and 1649+2635, which shows two radio jets and exhibits a clear spiral pattern (Mao et al. 2015; Singh et al. 2015). Detailed studies of these radio active late-type galaxies can advance our understanding of galaxy evolution and the triggering mechanism of their active galactic nuclei (AGNs).

In the last two decades, a few tens of Late-type Galaxies with double Radio Lobes (LaGRLs) have been discovered. Some of them are found by chance, such as NGC 612 (Emonts et al. 2008), Speca (Hota et al. 2011) and J2345−0449 (Bagchi et al. 2014). More LaGRLs are identified through systematic searches by combining data from optical and radio sky surveys, such as J1649+2635 (Mao et al. 2015) and J0836+0532 (Singh et al. 2015). Recently, Wu et al. (2022) expanded the existing sample by identifying 18 disks associated with radio lobes. In addition, Gao et al. (2023) discovered three new cases, J0326−0623, J1110+0321 and J1134+3046, by cross-matching a spiral sample derived by Kuminski & Shamir (2016) with the source catalogs of NRAO VLA Sky Survey (NVSS, Condon et al. 1998) and Faint Images of the Radio Sky at Twenty-centimeter (FIRST, Becker et al. 1995).

The observational characteristics of LaGRLs have been discussed in previous works. Emonts et al. (2008, 2009) found that NGC 612 and B2 0722+30 are HI-rich galaxies. Singh et al. (2015) indicated that J0836+0532 and J1352+3126 have a high star formation rate of 9.99 and 7.41 $M_\odot\,\mathrm{yr}^{-1}$ respectively, but belong to the AGN type based on their locations on the Baldwin-Phillips-Terlevich diagram (Baldwin et al. 1981). Wu et al. (2022) revealed that most disks in their sample are unusually red and massive (stellar mass $M_* \gtrsim 10^{11} M_\odot$), even though J1328+5710 is a blue dwarf galaxy with $M_* < 10^9 M_\odot$. Moreover, 0313−192 (Ledlow et al. 1998) and Speca (Hota et al. 2011) are found to be located in galaxy clusters.

It is not known why these disk galaxies can produce radio lobes. Singh et al. (2015) suggested that the radio lobes of J1159+5820 and J1352+3126 may result from galaxy mergers since the host galaxies display a disturbed disk and tidal tails. Wu et al. (2022) claimed that the mass of galaxy and then BH is a crucial factor in the formation of radio lobes. Gao et al. (2023) found that the surrounding environment may also play an important role because most (12/17) double-lobed spirals are found in galaxy groups or poor clusters.

To date, only about 30 LaGRLs have been identified (e.g., Wu et al. 2022; Gao et al. 2023), and most of the previous systematic searches (e.g., Mao et al. 2015; Singh et al. 2015; Wu et al. 2022; Gao et al. 2023) relied on optical samples derived from the Sloan Digital Sky Survey (SDSS, York et al. 2000). The Dark Energy Spectroscopic Instrument (DESI) imaging surveys (Dey et al. 2019), covering a larger sky region and having a deeper exposure than those of the SDSS, are publicly available recently (e.g., Zou et al. 2022). We therefore try to identify more LaGRLs by combining the data from DESI imaging surveys with those of NVSS and FIRST. We also aim to study the statistical properties of all known LaGRLs and speculate the formation mechanisms of their lobes.

The paper is organized as follows. In Section 2, we introduce the data sets and the search method and present the result. In Section 3, we perform statistical analysis on all known cases. We finally summarize in Section 4. We adopt a flat ΛCDM cosmology by assuming $H_0 = 70\,\mathrm{km\,s^{-1}\,Mpc^{-1}}$, $\Omega_\mathrm{m} = 0.3$ and $\Omega_\Lambda = 0.7$ throughout this paper.

2. Data Sets and Searching Strategy

2.1. Data Sets

The DESI imaging surveys consist of three independent surveys (Dey et al. 2019): the Dark Energy Camera Legacy Survey (DECaLS), the Beijing-Arizona Sky Survey (BASS, Zou et al. 2017) and the Mayall z-band Legacy Survey (MzLS). Additionally, the 6 yr imaging data from the Wide-field Infrared Survey Explorer (WISE, Wright et al. 2010; Schlafly et al. 2019) W1 (3.4 μm) and W2 (4.6 μm) bands are combined for all optically detected sources. The overall 5σ depths for each band are approximately $g = 24.7$ mag, $r = 23.9$ mag, $z = 23.0$ mag, W1 = 20.7 AB mag and W2 = 20.0 AB mag, respectively (Zou et al. 2022). The measured Full Widths at Half Maximum (FWHMs) of the point-spread function for the optical bands are less than 1.″7 (Dey et al. 2019). The 9th Data Release (DR9[4]) of the DESI survey covers a sky area of over 19,000 deg^2 for all the five bands and includes more than 320 million galaxies in total with $m_\mathrm{r} < 23.0$ mag (Zou et al. 2022).

The NRAO VLA Sky Survey[5] (NVSS) is conducted at 1.4 GHz and covers about 82% of the entire celestial sphere ($\delta > -40°$, Condon et al. 1998). The NVSS source catalog contains over 1.8 million discrete sources and becomes flux complete when $S_{1.4\,\mathrm{GHz}} > 2.5$ mJy. The NVSS images have an FWHM angular resolution of ∼45″ and a brightness rms of ∼0.45 mJy beam^{-1}. The position accuracy of NVSS is better than 1″ for sources stronger than 15 mJy and around 7″ at the survey limit. The FIRST[6] survey covers ∼10,000 deg^2 in the north and south galactic caps and also operates at 1.4 GHz (Becker et al. 1995). The FIRST survey has a higher angular resolution of 5″ better than that of NVSS and produces maps with a typical rms of 0.15 mJy. The position uncertainties for FIRST-detected sources are better than 0.″5 at 3 mJy level and approximately 1″ at the survey threshold. In this paper, we use the latest version of the FIRST catalog (version 14Dec17) within which 946,432 sources are included.

2.2. Searching Strategy

We begin with constructing a sample of disk galaxies based on the DESI database. Because edge-on disk galaxies appear to have a projected major axis much longer than their minor axis, we select galaxies by requiring a major-to-minor axis ratio larger than 4. This threshold allows us to pick up disk galaxies with a high purity, though many disks may be missed especially for the face-on spiral galaxies. Elliptical galaxies may appear disk-like if they are lensed by a foreground massive object. To avoid such possible contamination, optical images are examined. To guarantee the accuracy of the measurements toward galaxy morphology and parameters, we only take the bright galaxies by discarding faint ones with the r-band integrated apparent magnitude $m_\mathrm{r} \geqslant 19.5$ mag. As a result, 885,070 galaxies are included in the optical sample.

The NVSS data is taken as the primary radio database for cross-matching, mainly due to its more complete sky coverage (over 3 times) and better largest-angular-scale visible to the telescope array in comparison to those of the FIRST data. However, the limited angular resolution of NVSS images may make the verification of optical-radio association challenging, especially in dense regions like galaxy groups or clusters. Therefore, we use the FIRST images, if available, to further identify the potential associations between DESI and NVSS sources.

It is pivotal to adopt an optimal radius for optical-radio cross-matching since a small value would miss some large-scale lobes, while a large radius would produce an overwhelming number of fake associations. Based on the experience gained from previous works (Yuan et al. 2016; Gao et al. 2023), we set the cross-matching radius as 500 kpc. This radius is sufficiently large given that only one case, J2345−0449, is known to host radio lobes with a total length exceeding 1 Mpc. Nevertheless, for J2345−0449, we can still identify it through its radio emission encircled within the radius of 500 kpc. Unlike the method used by Gao et al. (2023), we do not impose any restrictions on the angles between radio sources to the central optical disk to avoid the omission of radio lobes with a bent or complex morphology.

After cross-matching was made in such a way, 104 candidates were found after visual inspection. We then overlay the DESI, NVSS and FIRST (if available) images for each candidate. The candidates undergo strict validation, and most of them are dismissed. For instance, (1) galaxies with an arc-like optical morphology are eliminated to prevent false identifications of lensed elliptical galaxies; (2) very weak radio

[4] https://www.legacysurvey.org/dr9/
[5] https://www.cv.nrao.edu/nvss/
[6] http://sundog.stsci.edu/

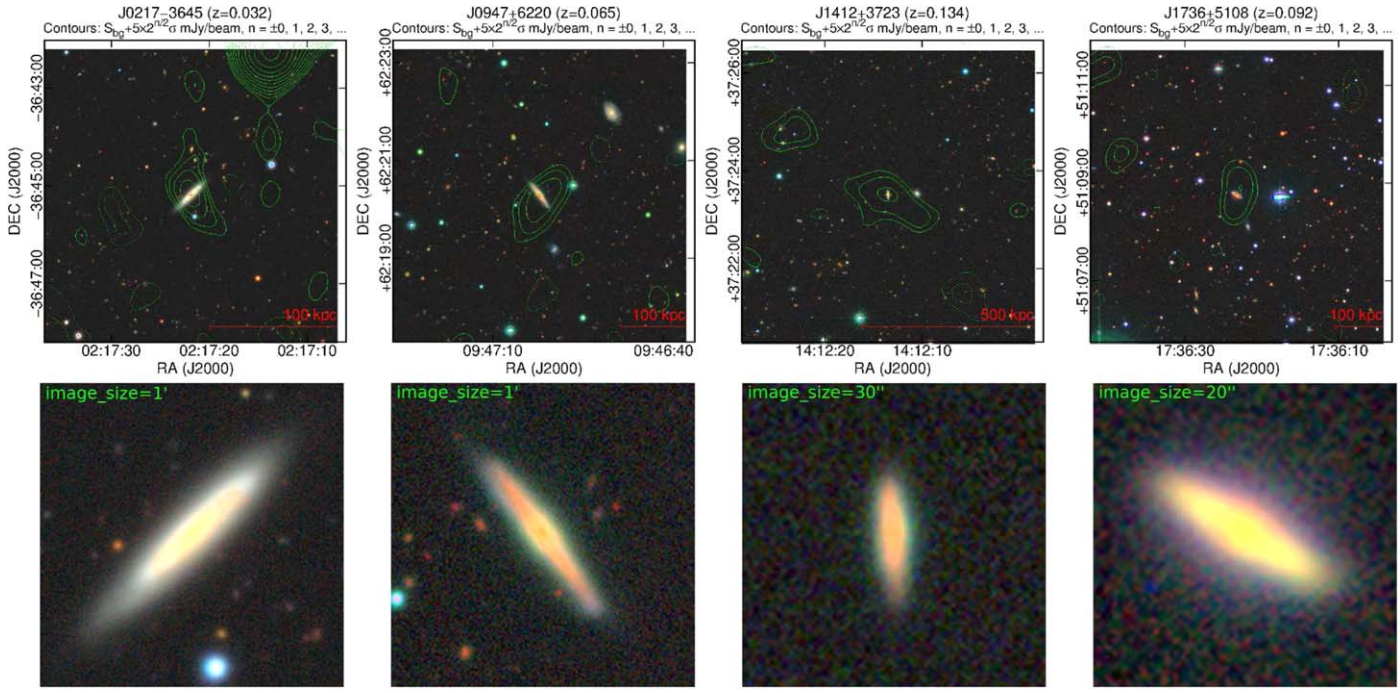

Figure 1. Upper panels: Optical (DESI) images with superimposed radio contours (green: NVSS; red: FIRST) for the four newly identified LaGRLs. The source name, redshift, and contour levels are marked on the top of each panel. S_{bg} and σ are the mean and rms of the radio background. The central cross denotes the position on the radio image corresponding to the optical center of the disk and is used to ensure the overlaying accuracy. The scale of 100 or 500 kpc is shown at the bottom-right corner of each panel. Lower panels: Zoomed-in DESI images for disks corresponding to that shown in the top panel. The size of each map is indicated at the top-left corner.

sources are not considered if the brightness peak detected by the NVSS is fainter than a signal-to-noise ratio of 10; (3) radio emissions that cannot be well distinguished from the disk galaxy or contaminated by a nearby foreground/background object are excluded; (4) no nearby optical contaminators exist, but the radio center detected by the NVSS deviates slightly from the optical center, and no FIRST data can be used for further verification. Finally, we get four new disk galaxies hosting radio lobes with high confidence. The composite images for the four sources are displayed in Figure 1, and their parameters are listed in Table 1.

2.3. Notes on New LaGRLs

2.3.1. J0217−3645

This galaxy is a bulgeless disk at $z = 0.032$ (Zou et al. 2022). The radio lobes of this galaxy cannot be resolved in the NVSS map but exhibit an elongated morphology that is perpendicular to the stellar disk. The size of the radio emission indicated by the NVSS 5σ contour is about 70 kpc. The radio brightness decreases gradually from the center to the edges, suggesting that this radio galaxy belongs to the Fanaroff-Riley I (FR-I) type (Fanaroff & Riley 1974). Unfortunately, this galaxy is not covered by the FIRST survey, so that high-resolution radio image is not available. Considering that no large galaxy is found in the vicinity and the radio peak coincides well with the optical center (see Figure 1), we suggest that the radio emission is intrinsically associated with this disk galaxy.

2.3.2. J0947+6220

J0947+6220 is a typical disk galaxy located at a redshift of 0.065. The radio emission from this galaxy exhibits an elongated morphology, extending along its minor axis to a size of ∼150 kpc. The superimposed image reveals that the galaxy is slightly offset from the center of NVSS contours. However, the FIRST survey detects a radio core that is well-associated with the center of the galaxy. Additionally, no other radio sources can be detected in the vicinity of the galaxy. Based on these findings, we believe that the diffuse radio emission detected by the NVSS originates from the galaxy.

2.3.3. J1412+3723

This galaxy is a disk-dominated galaxy located at $z = 0.134$. The total size of the radio emission, as indicated by the NVSS 5σ contour, is approximately 300 kpc. The radio morphology

Table 1
Parameters for 36 Late-type Galaxies with Double Radio Lobes

Name	Reference	R.A. (J2000)	Decl. (J2000)	z	$S_{\rm tot}$ (mJy)	$P_{1.4\ \rm GHz}$ (W Hz^{-1})	$\log_{10} M_*$ ($M_\odot$)	$M_{\rm g}$ (mag)	$M_{\rm r}$ (mag)	Env.	$N_{\rm nbr}$
(1)	(2)	(3)	(4)	(5)	(6)	(7)	(8)	(9)	(10)	(11)	(12)
J0133−3629	(1)	23.490 86	−36.49306	0.020	5137	4.29×10^{24}	10.81	−21.18	−22.01	group	8
J0209+0750	(2)	32.269 81	7.834 60	0.236	585	9.77×10^{25}	11.82	−23.18	−23.88	field	0
J0219+0155	(2)	34.994 69	1.930 12	0.034	560	1.39×10^{24}	11.04	−21.52	−22.39	group	2
J0315−1906	(3)	48.967 08	−19.11230	0.074	100	1.29×10^{24}	10.74	−20.66	−21.50	group	5
J0326−0623	(4)	51.599 28	−6.38433	0.149	6[a]	$3.54^{a} \times 10^{23}$	10.90	−22.31	−22.96	group	2
J0354−1340	(5)	58.636 81	−13.66888	0.051	15	9.01×10^{22}	10.68	−21.43	−22.09	group	3
J0725+2957	(6)	111.40515	29.954 08	0.033	150	3.69×10^{23}	10.78	−20.64	−21.55	group	2
J0802+1157	(2)	120.74894	11.952 73	0.186	21	2.04×10^{24}	10.65	−21.29	−21.93	group	1
J0806+0624	(2)	121.74416	6.414 81	0.103	5	1.31×10^{23}	9.56	−20.43	−20.85	group	0[d]
J0832+1848	(2)	128.10347	18.815 41	0.121	109	4.09×10^{24}	11.46	−22.22	−23.00	field[b]	0
J0836+0532	(7)	129.23279	5.545 00	0.059	62	4.95×10^{23}	11.08	−22.35	−23.03	group	2
J0847+1241	(2)	131.99957	12.699 79	0.163	11	7.97×10^{23}	11.64	−22.20	−23.08	group	3
J0855+4204	(2)	133.95479	42.072 25	0.210	177	2.25×10^{25}	11.03	−21.27	−22.07	group	4
J0914+4137	(2)	138.68979	41.620 62	0.130	474	2.08×10^{25}	11.58	−23.09	−23.96	group	4
J0926+4652	(2)	141.52162	46.876 09	0.235	11	1.81×10^{24}	11.07	−21.56	−22.49	field	0
J0956+1628	(2)	149.02443	16.475 04	0.374	87	4.30×10^{25}	11.54	−22.44	−23.16	group	3
J0958+5619	(2)	149.63934	56.327 16	0.258	259	5.31×10^{25}	11.39	−22.43	−23.17	group	1
J1110+0321	(4)	167.60457	3.360 79	0.028	587	9.76×10^{23}	9.41	−19.49	−19.96	group	3
J1128+2417	(2,4)	172.04846	24.296 36	0.100	69	1.70×10^{24}	9.93	−20.36	−20.84	group	3
J1134+3046	(4)	173.58467	30.779 57	0.040	380	1.38×10^{24}	9.95	−19.60	−20.15	field	0
J1159+5820	(4,7,8)	179.77362	58.343 24	0.047	338	1.66×10^{24}	11.11	−22.17	−22.92	field[b]	0
J1328+5710	(2)	202.03833	57.173 44	0.026	22	3.16×10^{22}	8.69	−18.39	−18.66	field[b]	0
J1352+3126	(4,7,9)	208.07425	31.446 29	0.035	4844	1.34×10^{25}	11.27	−21.93	−22.72	field[b]	0
J1409−0302	(4,10)	212.45355	−3.04239	0.124	139	5.46×10^{24}	11.54	−22.39	−23.22	group	11
J1633+0847	(2)	248.25356	8.793 49	0.264	36	7.76×10^{24}	11.35	−22.19	−22.95	group	1
J1646+3831	(2)	251.61842	38.521 10	0.076	393	5.44×10^{24}	10.68	−21.13	−21.90	group	3
J1649+2635	(4,7,11)	252.35013	26.584 03	0.042	157	6.11×10^{23}	11.43	−21.99	−22.81	group	5
J1656+6407	(2)	254.08594	64.131 36	0.189	75	7.50×10^{24}	11.57	−22.62	−23.34	group	3
J1721+2624	(2)	260.28290	26.408 94	0.142	255	1.35×10^{25}	11.22	−21.76	−22.48	group	4
J2141+0821	(2)	325.29419	8.359 02	0.324	122	4.29×10^{25}	10.82	−21.94	−22.69	group	4
J2318+4314	(12)	349.63650	43.246 92	0.012	17	5.20×10^{21}	...	...	...	group[c]	...
J2345−0449	(13)	356.38632	−4.82367	0.040	181	6.39×10^{23}	11.26	−22.59	−23.32	group	4
J0217−3645	(0)	34.339 29	−36.75179	0.032	4	9.13×10^{21}	10.28	−20.27	−21.10	field	0
J0947+6220	(0)	146.75429	62.339 57	0.065	3	2.96×10^{22}	10.61	−19.94	−20.95	group	2
J1412+3723	(0)	213.05438	37.393 07	0.134	3	1.39×10^{23}	10.79	−20.46	−21.32	group	2
J1736+5108	(0)	264.09451	51.147 23	0.092	...	...	10.96	−20.72	−21.59	field	0

Note. Columns (1–2): source name and reference. References are denoted by numbers, with (0) = this work; (1) = Emonts et al. (2008); (2) = Wu et al. (2022); (3) = Ledlow et al. (1998); (4) = Gao et al. (2023); (5) = Vietri et al. (2022); (6) = Emonts et al. (2009); (7) = Singh et al. (2015); (8) = Kozieł-Wierzbowska et al. (2012); (9) = van Breugel et al. (1984); (10) = Hota et al. (2011); (11) = Mao et al. (2015); (12) = Mulcahy et al. (2016); (13) = Bagchi et al. (2014). Columns (3–5): R.A., decl., and redshift of the galaxy, measured from the DESI image (Zou et al. 2022), except for J2318+4314, for which the parameters are obtained from the NASA/IPAC Extra-galactic Database (NED, http://ned.ipac.caltech.edu/). Column (6): total radio flux density measured by the NVSS, with a note "*a*" indicating contamination from an irrelevant source (see Gao et al. 2023). Column (7): radio power calculated with Equation (1). Columns (8–10): stellar mass, *g*-band and *r*-band absolute magnitude of the galaxy, taken from Zou et al. (2022). Columns (11–12): the environment where the galaxy is located and the number of neighboring galaxies, see Section 3.3 for details. "*b*"—the galaxy shows disturbed structures, "*c*"—uncovered by the DESI survey but validated by Mulcahy et al. (2016), "*d*"—the galaxy has a companion but fainter than −20.0 mag.

of this galaxy exhibits an inside-out decrease in radio brightness, which is a characteristic feature of the FR-I type. Although this galaxy is not covered by the FIRST survey, we can still infer that the radio emission originates from the disk galaxy because of the good match between the radio peak and optical galaxy.

2.3.4. J1736+5108

J1736+5108, at $z = 0.092$, hosts both a disk and a bulge component as indicated by the DESI zoomed-in image. The size of the radio emission indicated by the NVSS 5σ contour is $\sim$150 kpc. Despite a peak radio brightness over 10σ, the NVSS integrated flux density for this source is unavailable. The

FIRST survey detects a radio core that is associated with the galaxy, which confirms the authenticity of the radio emission detected by NVSS and further strengthens the reliability of the optical-radio association.

3. Properties of LaGRLs

In this part we discuss the properties of LaGRLs identified in this work together with the known objects in the previous literature.

3.1. Radio Power and Galaxy Mass

The radio lobes of galaxies are generated by their nuclei, suggesting a possible connection between their radio power and the mass of the central BHs, which is further correlated with the stellar mass of the host galaxies (e.g., Marconi & Hunt 2003; Gültekin et al. 2009). Wu et al. (2022) found that more luminous galaxies or those with a larger BH mass tend to host more powerful radio lobes. Similarly, Gao et al. (2023) examined this relation for 17 spiral galaxies and arrived at a consistent conclusion.

The NVSS is suitable for detecting diffuse radio lobes of galaxies due to its relatively short baseline. To estimate the power of radio lobes, we extract the radio flux density $S_{1.4\ \mathrm{GHz}}$ from the NVSS source catalog. In most cases, the radio structure in NVSS maps is simple and easy to distinguish. In the absence of contaminators, we extract the lobe flux from the total flux obtained from NVSS. In a few cases where the sources exhibit complex structures, we carefully examine the optical-radio overlaid image and sum the flux densities of all related components to obtain the total value. The radio power $P_{1.4\ \mathrm{GHz}}$ can be calculated following the equation:

$$P_{1.4\mathrm{GHz}} = 4\pi D_{\mathrm{L}}^2 \times S_{1.4\mathrm{GHz}} \times (1+z)^{1-\beta}. \quad (1)$$

Here, $D_{\mathrm{L}} = (1+z)\frac{c}{H_0}\int_0^z \frac{dz'}{\sqrt{\Omega_{\mathrm{m}}(1+z')^3+\Omega_{\Lambda}}}$ represents the luminosity distance, z is the redshift, and the term $(1+z)^{(1-\beta)}$ accounts for the k-correction. β is the spectral index of the power-law $S_\nu = \nu^{-\beta}$ and is assumed to be 0.74 based on the result of Lin & Mohr (2007), here ν is the frequency and S_ν is the flux density at ν. We do not quote the values of radio powers from existing literature, avoiding the potential bias caused by variations in telescopes or frequencies. The stellar masses of galaxies are estimated by Zou et al. (2022) based on the DESI imaging data.

In the top panel of Figure 2, we present the relation between the stellar mass of host galaxies and the power of their radio lobes for 33 LaGRLs with available data. Overall, the correlation between the power of radio lobes and the stellar

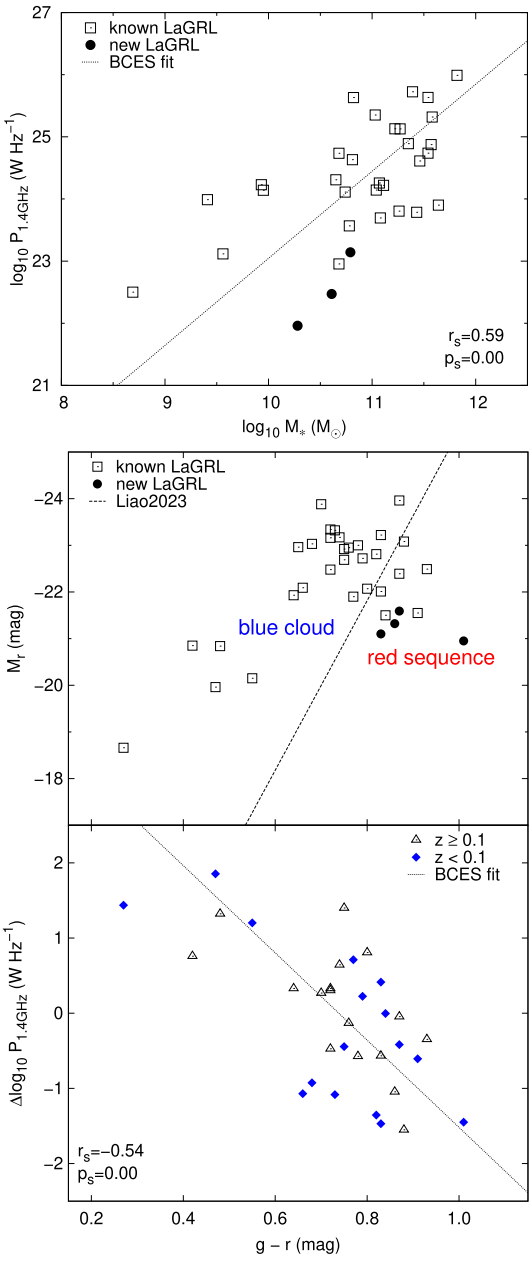

Figure 2. Top panel: The correlation between stellar mass and radio powers of 30 known (open-square) and three new (solid-circle) LaGRLs with available data. J0326−0623 is not used here due to flux contamination. The dotted line is the BCES best-fitted line for all sources. The values of the Spearman rank-order correlation coefficient r_s and the correlation significance p_s are shown at the bottom-right corner. Middle panel: The color—magnitude distribution for 31 known (open-square) and four new (solid-circle) LaGRLs. The dashed line is the fiducial separation between the red sequence and the blue cloud defined by Liao & Cooper (2023). Bottom panel: The galaxy color against the differential radio power, which is the offset from the power—mass relation shown in the top panel. LaGRLs with $z \geqslant 0.1$ are labeled as open triangles, while those with $z < 0.1$ are marked as solid diamonds. The dotted line is the BCES best-fitted line for all sources. The values of r_s and p_s are marked at the bottom-left corner.

mass of host galaxies follows the relation

$$\log_{10} P_{1.4\mathrm{GHz}} = (1.40 \pm 0.03)\log_{10} M_* + (9.04 \pm 0.36), \quad (2)$$

which is obtained through the Bivariate Correlated Errors and intrinsic Scatter (BCES) fitting method (see Akritas & Bershady (1996) and also the appendix of Yuan et al. (2015) for details). The Spearman rank-order coefficient r_s for this correlation is 0.59 and the relevant significance factor p_s is 0.00 (see definition in (Press et al. 1992, page 640)), indicating that the correlation is intrinsic, although the scattering of the data points is large somehow.

3.2. Galaxy Color

The color is one of the fundamental characteristics of a galaxy and is closely related to its star formation rate, which further correlates to its gas content. The activity of an AGN depends on the gas accretion process and, conversely, can regulate the distribution of gas within galaxies (see Fabian 2012, for a review). Therefore, it is interesting to investigate the relationship between the color and radio emission for LaGRLs.

We take the absolute magnitudes of galaxies in the g-band (M_g) and r-band (M_r) from Zou et al. (2022) based on the DESI imaging data. The $g-r$ color is therefore obtained as the difference between M_g and M_r, which have considered the k- and the Galactic extinction correction. In the middle panel of Figure 2, we show the distribution of the 31 known (open-square) and four new (solid-circle) LaGRLs on the magnitude —color diagram. The dashed line is the demarcation line between the red sequence and the blue cloud galaxies, which is defined by Liao & Cooper (2023) with the formula $(g-r) = -0.055M_r - 0.4$ based on the DESI imaging data. It is evident that most (25/35) LaGRLs are located in the region of blue clouds, while all the four newly identified disks along with a few other cases are redder and in the region for red sequence galaxies.

In the bottom panel of Figure 2, we present the relation between the galaxy color and the differential radio power $\Delta \log_{10} P_{1.4\,\mathrm{GHz}}$ for 30 known and three newly discovered LaGRLs with available data, here the differential radio power means the deviation of radio power from the stellar mass—radio power correlation and therefore can be calculated through $\Delta \log_{10} P_{1.4\,\mathrm{GHz}} = \log_{10} P_{1.4\,\mathrm{GHz}} - 1.40 \log_{10} M_* - 9.04$. A correlation is found between the galaxy color and the differential radio power with $r_s = -0.54$ and $p_s = 0.00$, which indicates, after deducting the impact of galaxy mass, bluer galaxies tend to host more powerful radio lobes when compared to redder ones. We suggest that the accretion of central BH in bluer galaxies is more efficient than that in redder galaxies, possibly because the blue ones contain more cold gas than the red galaxies. The Star Formation Rate (SFR) of galaxies depends on redshift (e.g., Karim et al. 2011; Lindholmer & Pimbblet 2019), which could influence the correlation between the galaxy color and the differential radio power. We check the correlation between galaxy color and redshift for our sample and find the Spearman rank-order correlation coefficient r_s between these two parameters is 0.00 and the correlation significance p_s is 0.99, indicating that no correlation is found between them. This may be the result of the relatively small redshift range of our sample. Moreover, we divide the LaGRLs into two sub-samples based on their redshifts and find no significant difference between the two sub-samples (see Figure 2).

3.3. Galaxy Environment

The radio emission of the massive BH at the center of a galaxy is influenced by the environment surrounding the galaxy. Best et al. (2007) discovered that central galaxies in clusters have a higher fraction of being radio-loud than satellite galaxies in the same mass range, likely due to their locations in the central dense environment. Springel et al. (2005) suggested that galaxy mergers or gravitational tides could significantly increase the accretion rate onto the central BH during special periods. The environment surrounding the rare LaGRLs has been discussed in previous works for some individual sources (e.g., Hota et al. 2011; Mao et al. 2015; Singh et al. 2015). To investigate this further, Gao et al. (2023) searched for neighboring galaxies around 17 LaGRLs using SDSS data. They employed the method developed by Wen et al. (2012) and found that the majority (12/17) of these spirals are located within a group or a poor cluster.

Here we identify the neighbors for the 36 LaGRLs listed in Table 1. We employed a similar method as Gao et al. (2023), but using the DESI database. Galaxies with a redshift difference of less than $0.04(1+z)$ and a projected distance of less than 500 kpc, rather than 1 Mpc in Gao et al. (2023), are considered as neighbors of the LaGRLs. To ensure that the identification is not biased by missing faint galaxies at high redshifts, we only included galaxies with an evolution-corrected absolute magnitude, denoted as M_r^e, brighter than -20.0 mag as neighbors. The evolution-corrected absolute magnitude, M_r^e, is estimated following $M_r^e = M_r + 1.16z$ (Wen & Han 2015). While ensuring completeness, the threshold of M_r has been reduced from the -20.5 mag used by Gao et al. (2023) to -20.0 mag to allow the inclusion of fainter neighbors.

We find that among the 36 LaGRLs in our sample, 27 LaGRLs are located within a group. This may indicate that the massive BHs are more active in the relatively dense environment in galaxy groups. Additionally, four out of the rest nine field galaxies exhibit disturbed morphology, see Table 1, which validates the expectation made by Springel et al. (2005) that the BH accretion rate can increase clearly during galaxy merger. Overall, we suggest that the peculiar radio emission observed in LaGRLs may be related to the

influence of the surrounding environment, such as the accretion of intra-group medium, the gravitational tide, or the merger of nearby galaxies.

4. Summary

By far, only about 30 LaGRLs have been identified. Previous systematic searches for LaGRLs have been made from optical samples derived from the SDSS (e.g., Mao et al. 2015; Wu et al. 2022; Gao et al. 2023). In this study, we derived a sample of disk galaxies from the DESI imaging survey, which provides deeper observations and wider sky coverage. We unveil four new disks hosting radio lobes. By doing statistics of the known LaGRLs, we have the following findings:

1. The correlation between the power of radio lobes and the stellar mass of the host galaxy is confirmed for all known sources.
2. Most (25/35) LaGRLs belong to the blue cloud galaxies, while only a few including the four newly identified LaGRLs exhibit a redder color, located in the region of the red sequence.
3. The galaxy color is correlated with the differential radio powers, which indicates that bluer galaxies tend to host more powerful radio lobes.
4. 31 out of 36 LaGRLs in our sample are either located in a galaxy group or displaying disturbed structures, suggesting that the environment may also play a crucial role in stimulating the formation of radio lobes in late-type galaxies.

Acknowledgments

We thank the anonymous referee for helpful comments which helped us to improve the paper. This work is partially supported by the National SKA Program of China (grant No. 2022SKA0120103) and the National Natural Science Foundation of China (Nos. 11 988 101 and 11 833 009, 12 073 036). Z.S.Y. obtains support from the science research grants from the China Manned Space Project (CMS-CSST-2021-A01, CMS-CSST-2021-B01). X.Y.G. acknowledges the financial support from the National Key R&D Program of China (No. 2021YFA1600401 and 2021YFA1600400) and the International Partnership Program of Chinese Academy of Sciences, grant No. 114A11KYSB20170044.

This research has made use of the NASA/IPAC Extragalactic Database, which is operated by the Jet Propulsion Laboratory, California Institute of Technology, under contract with the National Aeronautics and Space Administration. The National Radio Astronomy Observatory is a facility of the National Science Foundation operated under a cooperative agreement by Associated Universities, Inc. The Legacy Surveys consist of three individual and complementary projects: the Dark Energy Camera Legacy Survey (DECaLS; NOAO Proposal ID # 2014B-0404; PIs: David Schlegel and Arjun Dey), the Beijing-Arizona Sky Survey (BASS; NOAO Proposal ID # 2015A-0801; PIs: Zhou Xu and Xiaohui Fan), and the Mayall z-band Legacy Survey (MzLS; NOAO Proposal ID # 2016A-0453; PI: Arjun Dey). DECaLS, BASS and MzLS together include data obtained, respectively, at the Blanco Telescope, Cerro Tololo InterAmerican Observatory, National Optical Astronomy Observatory (NOAO); the Bok Telescope, Steward Observatory, University of Arizona; and the Mayall Telescope, Kitt Peak National Observatory, NOAO. The Legacy Surveys project is honored to be permitted to conduct astronomical research on Iolkam Du'ag (Kitt Peak), a mountain with particular significance to the Tohono O'odham Nation.

References

Akritas, M. G., & Bershady, M. A. 1996, ApJ, 470, 706
Bagchi, J., Vivek, M., Vikram, V., et al. 2014, ApJ, 788, 174
Baldwin, J. A., Phillips, M. M., & Terlevich, R. 1981, PASP, 93, 5
Becker, R. H., White, R. L., & Helfand, D. J. 1995, ApJ, 450, 559
Best, P. N., Kauffmann, G., Heckman, T. M., et al. 2005, MNRAS, 362, 25
Best, P. N., von der Linden, A., Kauffmann, G., Heckman, T. M., & Kaiser, C. R. 2007, MNRAS, 379, 894
Condon, J. J., Cotton, W. D., Greisen, E. W., et al. 1998, AJ, 115, 1693
Dey, A., Schlegel, D. J., Lang, D., et al. 2019, AJ, 157, 168
Emonts, B. H. C., Morganti, R., Oosterloo, T. A., et al. 2008, MNRAS, 387, 197
Emonts, B. H. C., Tadhunter, C. N., Morganti, R., et al. 2009, MNRAS, 396, 1522
Fabian, A. C. 2012, ARA&A, 50, 455
Fanaroff, B. L., & Riley, J. M. 1974, MNRAS, 167, 31P
Gao, X. Y., Yuan, Z. S., Han, J. L., Wen, Z. L., & Shan, S. S. 2023, RAA, 23, 035005
Gültekin, K., Richstone, D. O., Gebhardt, K., et al. 2009, ApJ, 698, 198
Hota, A., Sirothia, S. K., Ohyama, Y., et al. 2011, MNRAS, 417, L36
Karim, A., Schinnerer, E., Martínez-Sansigre, A., et al. 2011, ApJ, 730, 61
Keel, W. C., White, R. E. I., Owen, F. ., & Ledlow, M. . 2006, AJ, 132, 2233
Kozieł-Wierzbowska, D., Jamrozy, M., Zola, S., Stachowski, G., & Kuźmicz, A. 2012, MNRAS, 422, 1546
Kuminski, E., & Shamir, L. 2016, ApJS, 223, 20
Ledlow, M. J., Owen, F. N., & Keel, W. C. 1998, ApJ, 495, 227
Ledlow, M. J., Owen, F. N., Yun, M. S., & Hill, J. M. 2001, ApJ, 552, 120
Liao, L.-W., & Cooper, A. P. 2023, MNRAS, 518, 3999
Lin, Y.-T., & Mohr, J. J. 2007, ApJS, 170, 71
Lindholmer, M. O., & Pimbblet, K. A. 2019, A&A, 629, A7
Mao, M. Y., Owen, F., Duffin, R., et al. 2015, MNRAS, 446, 4176
Marconi, A., & Hunt, L. K. 2003, ApJL, 589, L21
Mulcahy, D. D., Mao, M. Y., Mitsuishi, I., et al. 2016, A&A, 595, L8
Press, W. H., Teukolsky, S. A., Vetterling, W. T., & Flannery, B. P. 1992, Numerical Recipes in FORTRAN. The art of Scientific Computing (Cambridge: Cambridge Univ. Press)
Schlafly, E. F., Meisner, A. M., & Green, G. M. 2019, ApJS, 240, 30
Singh, V., Ishwara-Chandra, C. H., Sievers, J., et al. 2015, MNRAS, 454, 1556
Springel, V., Di Matteo, T., & Hernquist, L. 2005, MNRAS, 361, 776
van Breugel, W., Heckman, T., Butcher, H., & Miley, G. 1984, ApJ, 277, 82
Véron-Cetty, M. P., & Véron, P. 2001, A&A, 375, 791
Vietri, A., Järvelä, E., Berton, M., et al. 2022, A&A, 662, A20
Wen, Z. L., & Han, J. L. 2015, ApJ, 807, 178
Wen, Z. L., Han, J. L., & Liu, F. S. 2012, ApJS, 199, 34
Wright, E. L., Eisenhardt, P. R. M., Mainzer, A. K., et al. 2010, AJ, 140, 1868
Wu, Z., Ho, L. C., & Zhuang, M.-Y. 2022, ApJ, 941, 95
York, D. G., Adelman, J., Anderson, J. E. J., et al. 2000, AJ, 120, 1579
Yuan, Z. S., Han, J. L., & Wen, Z. L. 2015, ApJ, 813, 77
Yuan, Z. S., Han, J. L., & Wen, Z. L. 2016, MNRAS, 460, 3669
Zou, H., Sui, J., Xue, S., et al. 2022, RAA, 22, 065001
Zou, H., Zhou, X., Fan, X., et al. 2017, PASP, 129, 064101